Stability, Unfolding, and Structural Changes of Cofactor-Free 1*H*-3-Hydroxy-4-oxoquinaldine 2,4-Dioxygenase

Bernd Beermann,[‡] Jessica Guddorf,[‡] Kristian Boehm,[‡] Alexander Albers,[§] Stephan Kolkenbrock,[§] Susanne Fetzner,[§] and H.-J. Hinz*[,‡]

Institut für Physikalische Chemie der WWU Münster, Corrensstrasse 30 and CeNTech, Heisenbergstrasse 11, 48149 Münster, Germany, and Institut für Molekulare Mikrobiologie und Biotechnologie der WWU Münster, Corrensstrasse 3, 48149 Münster, Germany

Received October 30, 2006; Revised Manuscript Received February 6, 2007

ABSTRACT: Stability, unfolding mechanism, spectroscopic, densimetric, and structural characteristics of the oxidatively stable C69S variant (HodC) of 1*H*-3-hydroxy-4-oxoquinaldine 2,4-dioxygenase (Hod) have been determined by classical and pressure modulation scanning calorimetry (DSC and PMDSC, respectively), circular dichroism (CD) spectroscopy, differential scanning densimetry (DSD), and dynamic light scattering measurements. At 25 °C, hexahistidine-tagged HodC has a hydrodynamic radius of 2.3 nm and is characterized by an unusually high degree of α-helical structure of ∼60%, based on deconvolution of CD spectra. The percentage of *β*-sheets and -turns is expected to be relatively low in view of its sequence similarity to proteins of the α/*β*-hydrolase fold superfamily. His_6HodC exhibits three-state unfolding (N ↔ I ↔ D) with an intermediate state I that exhibits at the transition temperature a volume larger than that of the native or denatured state. The intermediate state I is also associated with the highest isothermal expansion coefficient, α_P, of the three states and exhibits a significantly lower percentage of α-helical structure than the native state. The stability difference between the native and intermediate state is rather small which makes I a potential candidate for reactions with various ligands, particularly those having a preference for the apparently preserved *β*-type motifs.

1*H*-3-Hydroxy-4-oxoquinaldine 2,4-dioxygenase (Hod) from *Arthrobacter nitroguajacolicus* strain Rü61a is a catabolic enzyme involved in the pathway of quinaldine (2-methylquinoline) utilization. It catalyzes the 2,4-dioxygenolytic cleavage of 1*H*-3-hydroxy-4-oxoquinaldine, resulting in formation of carbon monoxide and *N*-acetylanthranilate. The reaction has been proposed to follow an ordered ternary complex mechanism, in which binding of the heteroaromatic substrate precedes dioxygen binding, and carbon monoxide is released as the first product (*1*). Hod is a dioxygenase without a requirement for cofactors or metal ions, which on the basis of sequence alignments and secondary structure predictions has been classified as a member of the α/*β*-hydrolase fold superfamily (*2*−*4*).

As the enzyme is of considerable scientific and practical interest, we present here the first part of an extensive thermodynamic characterization with emphasis on stability and unfolding properties. We include also CD studies, densimetric measurements, dynamic light scattering data, and pressure modulation DSC to complement the thermodynamic parameters with volumetric and structural information. These data will provide a sound basis for subsequent studies on the interaction with physiological and synthetic substrates in an evaluation of the thermodynamic and kinetic determinants of the energy−structure−function relationships of the reaction mechanism. Furthermore, the thermodynamic properties could be of value for optimizing crystallization conditions for the determination of the X-ray structure. To facilitate preparation and to avoid problems of intermolecular disulfide bridging, a His_6Hod protein carrying a cysteine 69 to serine substitution, designated His_6HodC, was used in this study. Since HodC in contrast to wild-type Hod is not susceptible to oxidative dimerization, it remains stable in its monomeric form (*1*). The His_6HodC protein consists of 288 amino acids and has a molar mass of 33 240.4 g/mol. It contains nine tryptophans, 10 tyrosines, and 11 phenylalanines that contribute to the absorbance at 280 nm and the near-UV CD signal.

MATERIALS AND METHODS

Protein Preparation

Bacterial Strain and Growth Conditions. Escherichia coli M15 [pREP4] pQE30-hodC69S (*3*) was grown in Luria-Bertani medium (LB) (*5*) in the presence of ampicillin (100 *μ*g/mL) and kanamycin (25 *μ*g/mL) at 37 °C. At an optical density (OD_{600}) of 0.5, gene expression was induced by addition of 0.5 mM isopropyl *β*-D-thiogalactopyranoside (IPTG), and the cultivation temperature was decreased to 20 °C. Cells were harvested after induction for 14 h at an OD_{600} of ∼3.2 by centrifugation at 10000*g* and 4 °C for 10 min. The yield of wet biomass of *E. coli* M15 [pREP4 pQE30-hodC69S] from a 5 L bioreactor was ∼26 g.

* To whom correspondence should be addressed. E-mail: hinz@uni-muenster.de.

[‡] Institut für Physikalische Chemie der WWU Münster.

[§] Institut für Molekulare Mikrobiologie und Biotechnologie der WWU Münster.

10.1021/bi0622423 CCC: $37.00
Published on Web 03/20/2007

Enzyme Assay, Preparation of Cell Extracts, and Purification of Recombinant His_6HodC. 1*H*-3-Hydroxy-4-oxoquinaldine, the organic substrate of Hod, was synthesized from 3-formyl-2-methyl-4(1*H*)-quinolone (*6*) as described by Cornforth and James (*7*). The catalytic activity of His_6HodC was determined spectrophotometrically by measuring substrate consumption as described previously (*1*).

For the purification of His_6HodC, 18 g of cells (wet biomass) of *E. coli* M15 [pREP4 pQE30-hodC69S] was suspended in 30 mL of 50 mM sodium phosphate buffer (pH 8.0) containing 10 mM imidazole and 300 mM NaCl. Crude extract, containing the soluble proteins, was obtained by sonication (UP200s sonifier, Dr. Hilscher GmbH, Stuttgart, Germany) and subsequent centrifugation at 40000*g* and 4 °C for 40 min. The supernatant was applied to a Ni^{2+}-nitrilotriacetate (Ni-NTA) agarose column (Qiagen, Hilden, Germany; 10 mL bed volume in a Bio-Scale MT10 column from BioRad Laboratories, Munich, Germany) equilibrated in 50 mM sodium phosphate buffer (pH 8.0) containing 10 mM imidazole and 300 mM NaCl. After the column had been washed with the same buffer and after application of a linear gradient (10.7 mL) of 20 to 55 mM imidazole, His_6-HodC was eluted by washing the column with 10 mL of 57 mM imidazole in equilibration buffer. Fractions containing His_6HodC were pooled and washed in 50 mM Tris-HCl (pH 8.0) by ultrafiltration (Vivaspin 20, molecular weight cutoff of 10 000; Vivascience, Hannover, Germany). The protein solution (5 mL) was loaded onto an UNO Q6 column equilibrated with the same buffer (6 mL bed volume; Bio-Rad). After a washing step followed by a linear gradient (9 mL) from 0 to 90 mM NaCl in 50 mM Tris-HCl buffer (pH 8.0), the column was washed with 12 mL of 90 mM NaCl in equilibration buffer to elute the His_6HodC protein. Fractions containing enzymatic activity were washed and concentrated in 10 mM sodium phosphate buffer (pH 7.5) by ultrafiltration at 4 °C. The protein was finally dialyzed three times for at least 4 h against 10 mM sodium phosphate buffer (pH 7.5).

The purity of the protein preparations was verified by denaturing (sodium dodecyl sulfate) polyacrylamide gel electrophoresis (*8*) and Coomassie staining. The specific activity of His_6HodC, determined in 50 mM Tris-HCl buffer (pH 8), corresponds to that of the HodC protein [~70 units/mg (*1*)].

UV Spectroscopy

Protein concentrations were determined by absorption measurements at 280 nm using an X-Dap (1024) diode array spectrophotometer from IKS. The extinction coefficient (ϵ) of 1.937 mL mg^{-1} cm^{-1} was calculated for His_6HodC according to the method of Pace et al. (*9*). Molar concentrations were calculated using an *M* of 33 240.4 g/mol.

Circular Dichroism Spectroscopy

CD spectra were recorded using a Jobin-Yvon (Paris, France) model CD-6 spectropolarimeter equipped with a Peltier-thermostated cell holder, constructed by the machine shop of the Institute of Physical Chemistry of the University of Münster.

The Peltier temperature control unit allows heating rates between 0.01 and 2.5 K/min. Cooling scans were performed using the same rates with the exception that the maximal cooling rate is limited to 1.3 K/min. The temperature is controlled to a precision of ±0.1 K. Quartz cells with an optical path length of 0.01 cm were used for protein concentrations in the range of 1 mg/mL and 1 cm cells for low concentrations of 0.05 mg/mL.

The results were expressed as mean residue ellipticity, $[\Theta]_{MRE} = (MRW\theta_{obs})/(cd)$, where θ_{obs} is the observed ellipticity at the respective wavelength, MRW (115.4 g/mol) is the mean residue weight of His_6HodC, *d* is the optical path length of the cell in centimeters, and *c* is the specific concentration (in milligrams per milliliter) of the samples.

Dynamic Light Scattering

All light scattering experiments were performed using a DynaPro molecular sizing instrument (Wyatt Technology) which operates at a fixed angle of 90°. The Dynamics 6.7.6 software package was used for data analysis. The translational diffusion coefficient, D_t, of the sample particles is determined by measuring the fluctuations in the intensity of the scattered light with an autocorrelator.

The hydrodynamic radius, r_H, of the particles was calculated using the Stokes−Einstein equation $D_t = (k_B T)/(6\pi\eta r_H)$, where k_B is the Boltzmann constant, *T* is the absolute temperature in kelvin, and η is the solvent viscosity.

All sample solutions for DLS measurements were filtered through a 0.2 μm filter (Anodisc 13; Whatman) before being used. Protein was in equilibrated buffer, and the concentration was adjusted to 1 mg/mL.

Differential Scanning Densimetry

Density measurements between 20 and 80 °C were performed in differential mode using two coupled high-temperature DMA 602 HT cells and a DMA 60 control unit of Anton Paar (Graz, Austria). Temperature scanning was controlled by a Haake PG 20 temperature controller. This arrangement reduces the influence of temperature fluctuations, as both cells are affected simultaneously. To collect data under isothermal conditions, heating was stopped every 0.4 °C, and after temperature equilibration, a defined number of oscillations were counted. The heating rate between the equilibration periods was 1 K/min. Calibration of the DSD instrument was conducted using pure water and air as reference systems. Counting of 20 000 oscillations had a time resolution of 2×10^{-6} s.

Differential Scanning Calorimetry

The heat capacity was determined using a model 6100 NanoDifferential scanning microcalorimeter (N-DSC) from Calorimetry Science Corp. (Spanish Fork, UT). The volume of both the sample cell and the reference cell is 299 μL. Various heating and cooling rates between 0.2 and 2.0 K/min were employed in these studies to check for kinetic effects on the heat capacity curves. A response time (τ) of the calorimeter of 9 s was selected for all experiments. All measurements were carried out in 10 mM sodium phosphate buffer (pH 7.5) using protein concentrations between 1.0 and 3.0 mg/mL. Measurements at constant pressure were performed by applying an excess pressure (*p*) of 3.5 bar.

Pressure Modulation DSC (PMDSC)

Theory and practice of pressure modulation calorimetry have recently been published (*10*, *11*). For the studies

presented here, we used the pressure control unit described in the papers cited above. The noise level of a scan with a constant pressure is less than 15 nW, and the reproducibility with or without refilling the cells is on the order of 1.7 μJ/K. For the studies on His_6HodC, we applied a sequence of continuous sawtooth-like pressure ramps between 0.3 and 5.3 bar excess pressure. A rate of pressure change of 0.031 bar/s together with a sampling rate of pressure and heat capacity values of 1 s^{-1} were routinely employed. The heating rate was 1 K/min for protein and buffer scans.

Transition Models Used in Data Analysis

For all models, the following procedure was identical. The change in standard Gibbs energy, $\Delta G°(T)$, was calculated at the assumption of temperature-dependent heat capacities ($C_p°$) of all states of the protein. The linear temperature dependence of the heat capacity was assumed for the native state and the intermediate state, whereas the temperature dependence of the heat capacity of the denatured state was fitted to a polynomial of second order, which was found to be appropriate in previous model studies on tripeptides (*12*−*14*). Therefore, the heat capacity difference between the native and denatured forms or the native and intermediate forms of the protein is a function of temperature itself and is designated by $\Delta C_p°(T)$. At the transition temperature T_m, the value is $\Delta C_p°(T_m)$, but as the $\Delta C_p°(T)$ curve has a slope, at T_m first and second derivatives with non-zero values exist. We refer to them as $\partial/\partial T[\Delta C_p°(T_m)]$ for the first derivative and as $\partial^2/\partial T^2[\Delta C_p°(T_m)]$ for the second derivative with regard to temperature. When only excess heat capacities are reported, such parameters are lost by routine baseline subtractions. We rather prefer to report the apparent heat capacities of the systems and the corresponding nonlinear variations of the baselines to allow for later theoretical calculations.

Two-State Model ($N \leftrightarrow D$). T_m is the temperature of the midpoint of the transition where the fractions of the native state and the denatured state are equal. $\Delta H°(T_m)$ and $\Delta C_p°(T_m)$ are the enthalpy and heat capacity difference between the two states at T_m, respectively. The expressions $\partial/\partial T[\Delta C_p°(T_m)]$ and $\partial^2/\partial T^2[\Delta C_p°(T_m)]$ refer to the first and second temperature derivatives of the function $\Delta C_p°(T)$, respectively, at T_m. $K(T)$ is the temperature-dependent equilibrium constant, and $f_D(T)$ is the temperature-dependent fraction of the denatured state.

Calculation of $\Delta G°(T)$:

$$\Delta G°(T) = \Delta H°(T_m)\left(1 - \frac{T}{T_m}\right) + \Delta C_p°(T_m)\left[T - T_m - \ln\left(\frac{T}{T_m}\right)\right] + \frac{\partial}{\partial T}\Delta C_p°(T_m)\left[\frac{{T_m}^2 - T^2}{2} + TT_m \ln\left(\frac{T}{T_m}\right)\right] + \frac{1}{2}\frac{\partial^2}{\partial T^2}\Delta C_p°(T_m)\left[\frac{{T_m}^3 - T^3}{3} + \frac{(T - T_m)(TT_m - T^2)}{2} - {T_m}^2 \ln\left(\frac{T}{T_m}\right)\right] \quad (1)$$

$$K(T) = e^{-\frac{\Delta G°(T)}{RT}} \quad (2)$$

$$f_D(T) = \frac{K(T)}{K(T) + 1} \quad (3)$$

Calculation of $\Delta H°(T)$:

$$\Delta H°(T) = \Delta H°(T_m) + \Delta C_p°(T_m)(T - T_m) + \frac{1}{2}\frac{\partial}{\partial T}\Delta C_p°(T_m)(T - T_m)^2 + \frac{1}{6}\frac{\partial^2}{\partial T^2}\Delta C_p°(T_m)(T - T_m)^3 \quad (4)$$

Calculation of $\Delta C_p°(T)$:

$$\Delta C_p°(T) = \Delta C_p°(T_m) + \frac{\partial}{\partial T}\Delta C_p°(T_m)(T - T_m) + \frac{1}{2}\frac{\partial^2}{\partial T^2}\Delta C_p°(T_m)(T - T_m)^2 \quad (5)$$

Calculation of $C_p°(T)$:

$$C_p°(T) = C_p°(N,T_m) + \frac{\partial}{\partial T}C_p°(N,T_m)(T - T_m) + \Delta C_p°(T)f_D(T) + \frac{\Delta H°(T)^2}{RT^2}[1 - f_D(T)]f_D(T) \quad (6)$$

Model of Two Independent Two-State Transitions ($N \leftrightarrow D_1$ and $N \leftrightarrow D_2$). For this model, two independent $\Delta G_i°(T)$ equations must be assumed that apply to the two independent transitions identified by the indices $i = 1$ and $i = 2$.

Calculation of $\Delta G_i°(T)$:

$$\Delta G_i°(T) = \Delta H_i°(T_{m,i})\left(1 - \frac{T}{T_{m,i}}\right) + \Delta C_{p,i}°(T_{m,i})\left[T - T_{m,i} - \ln\left(\frac{T}{T_{m,i}}\right)\right] + \frac{\partial}{\partial T}\Delta C_{p,i}°(T_{m,i})\left[\frac{{T_{m,i}}^2 - T^2}{2} + TT_{m,i} \ln\left(\frac{T}{T_{m,i}}\right)\right] + \frac{1}{2}\frac{\partial^2}{\partial T^2}\Delta C_{p,i}°(T_{m,i})\left[\frac{{T_{m,i}}^3 - T^3}{3} + \frac{(T - T_{m,i})(TT_{m,i} - T^2)}{2} - {T_{m,i}}^2 \ln\left(\frac{T}{T_{m,i}}\right)\right] \quad (7)$$

$$K_i(T) = e^{-\frac{\Delta G_i°(T)}{RT}} \quad (8)$$

$$f_{D,i}(T) = \frac{K_i(T)}{K_i(T) + 1} \quad (9)$$

Calculation of $\Delta H°(T)$:

$$\Delta H_i°(T) = \Delta H_i°(T_{m,i}) + \Delta C_{p,i}°(T_{m,i})(T - T_{m,i}) + \frac{1}{2}\frac{\partial}{\partial T}\Delta C_{p,i}°(T_{m,i})(T - T_{m,i})^2 + \frac{1}{6}\frac{\partial^2}{\partial T^2}\Delta C_{p,i}°(T_{m,i})(T - T_{m,i})^3 \quad (10)$$

Calculation of $\Delta C_p^\circ(T)$:

$$\Delta C_{p,i}^\circ(T) = \Delta C_{p,i}^\circ(T_{m,i}) + \frac{\partial}{\partial T}\Delta C_{p,i}^\circ(T_{m,i})(T - T_{m,i}) + \frac{1}{2}\frac{\partial^2}{\partial T^2}\Delta C_{p,i}^\circ(T_{m,i})(T - T_{m,i})^2 \quad (11)$$

The $C_p^\circ(T)$ curve is calculated taking both transitions into account:

$$C_p^\circ(T) = C_p^\circ(N,T_m) + \frac{\partial}{\partial T}C_p^\circ(N,T_m)(T - T_m) + f_{D,1}(T)\Delta C_{p,1}^\circ(T) + f_{D,2}(T)\Delta C_{p,2}^\circ(T) + \frac{\Delta H_1^\circ(T)^2}{RT^2}[1 - f_{D,1}(T)]f_{D,1}(T) + \frac{\Delta H_2^\circ(T)^2}{RT^2}[1 - f_{D,2}(T)]f_{D,2}(T) \quad (12)$$

Sequential Three-State Model (N ↔ I ↔ D). In this model, the index 1 refers to the N ↔ I transition and the index 2 to the I ↔ D transition. Properties referring to a single state are denoted with an index: N for native, I for intermediate, and D for denatured. Calculation of $\Delta G^\circ(T)$:

$$\Delta G_1^\circ(T) = \Delta H_1^\circ(T_{m,1})\left(1 - \frac{T}{T_{m,1}}\right) + \Delta C_{p,1}^\circ(T_{m,1})\left[T - T_{m,1} - \ln\left(\frac{T}{T_{m,1}}\right)\right] + \frac{\partial}{\partial T}\Delta C_{p,1}^\circ(T_{m,1})\left[\frac{{T_{m,1}}^2 - T^2}{2} + TT_{m,1}\ln\left(\frac{T}{T_{m,1}}\right)\right] \quad (13)$$

$$\Delta G_2^\circ(T) = \Delta H_2^\circ(T_{m,2})\left(1 - \frac{T}{T_{m,2}}\right) + \Delta C_{p,2}^\circ(T_{m,2})\left[T - T_{m,2} - \ln\left(\frac{T}{T_{m,2}}\right)\right] + \frac{\partial}{\partial T}\Delta C_{p,2}^\circ(T_{m,2})\left[\frac{{T_{m,2}}^2 - T^2}{2} + TT_{m,2}\ln\left(\frac{T}{T_{m,2}}\right)\right] + \frac{1}{2}\frac{\partial^2}{\partial T^2}\Delta C_{p,2}^\circ(T_{m,2})\left[\frac{{T_{m,2}}^3 - T^3}{3} + \frac{(T - T_{m,2})(TT_{m,2} - T^2)}{2} - {T_{m,2}}^2\ln\left(\frac{T}{T_{m,2}}\right)\right] \quad (14)$$

$$K_1(T) = e^{-[\Delta G_1^\circ(T)]/(RT)}\ K_2(T) = e^{-[\Delta G_2^\circ(T)]/(RT)} \quad (15)$$

$$f_N(T) = \frac{1}{K_2(T)K_1(T) + K_1(T) + 1}$$

$$f_I(T) = \frac{K_1(T)}{K_2(T)K_1(T) + K_1(T) + 1}$$

$$f_D(T) = \frac{K_2(T)K_1(T)}{K_2(T)K_1(T) + K_1(T) + 1} \quad (16)$$

Calculation of $\Delta H^\circ(T)$:

$$\Delta H_1^\circ(T) = \Delta H_1^\circ(T_{m,1}) + \Delta C_{p,1}^\circ(T_{m,1})(T - T_{m,1}) + \frac{1}{2}\frac{\partial}{\partial T}\Delta C_{p,1}^\circ(T_{m,1})(T - T_{m,1})^2 \quad (17)$$

$$\Delta H_2^\circ(T) = \Delta H_2^\circ(T_{m,2}) + \Delta C_{p,2}^\circ(T_{m,2})(T - T_{m,2}) + \frac{1}{2}\frac{\partial}{\partial T}\Delta C_{p,2}^\circ(T_{m,2})(T - T_{m,2})^2 + \frac{1}{6}\frac{\partial^2}{\partial T^2}\Delta C_{p,2}^\circ(T_{m,2})(T - T_{m,2})^3 \quad (18)$$

Calculation of $\Delta C_p^\circ(T)$:

$$\Delta C_{p,1}^\circ(T) = \Delta C_{p,1}^\circ(T_{m,1}) + \frac{\partial}{\partial T}\Delta C_{p,1}^\circ(T_{m,1})(T - T_{m,1}) \quad (19)$$

$$\Delta C_{p,2}^\circ(T) = \Delta C_{p,2}^\circ(T_{m,2}) + \frac{\partial}{\partial T}\Delta C_{p,2}^\circ(T_{m,2})(T - T_{m,2}) + \frac{\partial^2}{\partial T^2}\Delta C_{p,2}^\circ(T_{m,2})(T - T_{m,2})^2 \quad (20)$$

The complete $C_p^\circ(T)$ curve is then calculated using the following equation:

$$C_p^\circ(T) = C_p^\circ(N,T_{m,1}) + \frac{\partial}{\partial T}C_p^\circ(N,T_{m,1})(T - T_{m,1}) + \Delta C_{p,1}^\circ(T)[f_I(T) + f_D(T)] + \Delta C_{p,2}^\circ(T)f_D(T) + \frac{\Delta H_1^\circ(T)^2}{RT^2}f_N(T)[f_I(T) + f_D(T)] + \frac{\Delta H_2^\circ(T)^2}{RT^2}[f_N(T) + f_I(T)]f_D(T) + 2\frac{\Delta H_1^\circ(T)\Delta H_2^\circ(T)}{RT^2}f_N(T)f_D(T) \quad (21)$$

The fractions $f_N(T)$, $f_I(T)$, and $f_D(T)$ are calculated using eqs 13−16.

Nonthermodynamic properties of the protein [$X(T)$], such as density and CD spectroscopic signals, were assumed to be additive, and they were analyzed according to the following equation:

$$X(T) = f_N(T)X_N(T) + f_I(T)X_I(T) + f_D(T)X_D(T) \quad (22)$$

where $X_N(T)$, $X_I(T)$, and $X_D(T)$ refer to the temperature-dependent properties of the pure states and $f_N(T)$, $f_I(T)$, and $f_D(T)$ are the fractions of the pure species N, I, and D, respectively, occurring at the respective temperature. They were also calculated using eqs 13−16 and the thermodynamic parameters obtained from DSC.

RESULTS AND DISCUSSION

Structural Characterization of His_6HodC via CD Spectroscopy

As no X-ray or NMR structure is available for Hod, it is of particular interest to provide a quantitative CD analysis of the secondary and tertiary structure of the His_6HodC protein. Figure 1A shows spectra of the native and denatured states of the protein from 180 to 260 nm at 25 and 75 °C, respectively. The ordinate refers to mean residue ellipticities based on an M_{res} of 115.4 g/residue.

The far-UV region is characteristic of secondary structural motifs such as α-helices, β-sheets, and β-turns. Using the software of Böhm et al. (*15*), the deconvolution of the native spectrum indicates a high degree of α-helicity of 60% and a relatively low content of β-structural elements (Table 1).

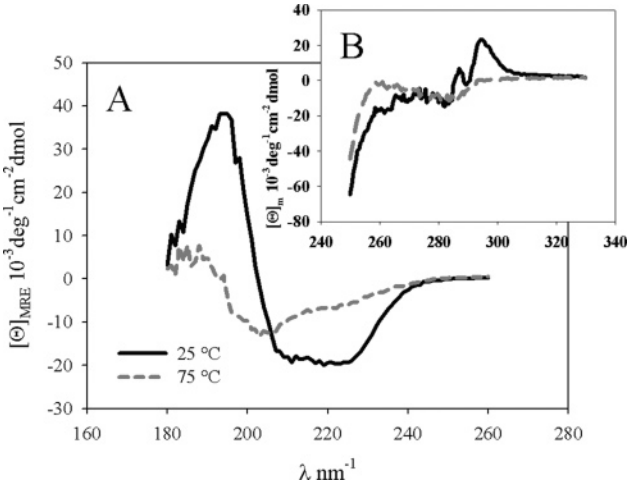

FIGURE 1: CD spectra of His_6HodC. (A) Far-UV CD spectra of His_6HodC at 25 (—) and 75 °C (– – –) in 10 mM sodium phosphate buffer (pH 7.5). The data are given as mean residue ellipticities. The spectrum shown is the average of 10 spectra. It was recorded in a 0.1 mm cuvette at a protein concentration of 1.06 mg/mL. The integration time was 1 s. (B) CD spectra of His_6-HodC in the near-UV region at 25 (—) and 75 °C (– – –) in 10 mM sodium phosphate buffer (pH 7.5). The values are given as molar ellipticities (M = 33 240.4 g/mol). The spectrum shown is the average of 10 spectra and was recorded in a 1.0 cm cuvette at a protein concentration of 1 mg/mL. The integration time was 1 s.

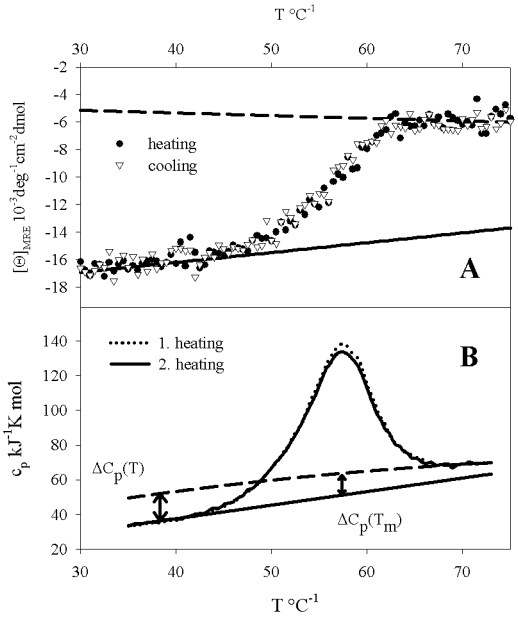

FIGURE 2: Repeatability test for the unfolding of His_6HodC. (A) Sequential heating and cooling curves monitored by CD spectroscopy at 222 nm. The sample concentration was 1.06 mg/mL. The transition curves were recorded in a 0.1 mm cuvette at a heating rate of 2 K/min and a cooling rate of 1 K/min. The integration time per data point was 2 s each: (—) native state and (– – –) denatured state. (B) Two subsequent heat capacity curves of a 1.06 mg/mL protein solution in 10 mM sodium phosphate (pH 7.5). The heating rate was 2 K/min. Cooling was started immediately after a temperature of 66 °C had been reached: (—) native state and (– – –) denatured state.

This result is particularly surprising, as sequence alignments showed a reasonable degree of homology with proteins belonging to the α/β-hydrolase fold superfamily (*2*, *3*). Among the α/β-hydrolases described in the Protein Data Bank, epoxide hydrolase from *Agrobacterium radiobacter* AD1 (*16*) (PDB entry 1EHY) is most similar in sequence to Hod (28.1% identical and 38.8% similar). However, the protein has in comparison to HodC only 42.5% α-helical motifs but ~16% β-structure.

Figure 1B shows the near-UV CD spectrum from 250 to 330 nm of the native (25 °C) and unfolded (75 °C) protein. Here we report molar ellipticities (M = 33 240.4 g/mol) as the signal results from the difference in absorption of left and right circularly polarized light of the aromatic residues only, and calculation of MRE values would be meaningless.

The spectrum of the native protein exhibits two prominent peaks at 285 and 294 nm which are characteristic of tertiary structure. They clearly indicate a stable, asymmetric arrangement of several Trp, Tyr, and Phe residues in the native molecule. Both peaks disappear upon heating to 75 °C, which demonstrates the complete loss of tertiary structure at this temperature.

Thermal Unfolding

Thermal unfolding was monitored by DSC, PMDSC, CD, and DSD. With each method, we observed nearly complete reversibility (>98%) of the unfolding signals when samples were heated to 66 °C followed by immediate cooling to a temperature below the transition. This is demonstrated in Figure 2 for typical CD and DSC measurements.

Such a high degree of reversibility is rather unusual for proteins of this size, although in recent DSC studies on chitinase 40 an equally high degree of reversibility was reported (*17*).

Heating His_6HodC to temperatures higher than 66 °C resulted in a decrease in reversibility, i.e., a decrease in peak height in DSC and a reduced transition amplitude of the CD signal (data not shown). However, it is worth noting that refolding was accompanied by a corresponding recurrence of catalytic activity. Even after five cycles of heating and cooling between 20 and 72 °C followed by one cycle between

Table 1: Results of the Deconvolution of the CD Spectrum at 25 °C of His_6HodC in 10 mM Sodium Phosphate Buffer (pH 7.5)[a]

	180−260 nm	185−260 nm	190−260 nm	195−260 nm	200−260 nm	205−260 nm	210−260 nm	mean	deviation
α-helix content (%)	46.6	59.5	59.6	63.4	64.7	65.2	64.1	60.4	±*6.4*
antiparallel β-sheet content (%)	2.7	3.8	0.2	1.6	3.4	3.5	3.5	2.7	±*1.3*
parallel β-sheet content (%)	9.8	6.6	6.3	5.8	5.6	5.3	5.3	6.4	±*1.6*
β-turn content (%)	11.4	12.1	10.8	10.3	10.4	11.0	12.3	11.2	±*0.8*
aperiodic structure content (%)	19.6	19.3	20.7	19.6	19.7	19.6	20.0	19.8	±*0.5*
sum (%)	90.1	101.4	97.6	100.6	103.7	104.6	105.2	100.5	±*5.3*

[a] The deconvolution software was CDNN by Böhm et al. (*15*).

20 and 80 °C, one observes 79% of original activity that corresponds well to a percentage of refolding of 76%.

As sometimes transition parameters and particularly the transition temperature can vary with heating rate as the result of slow unfolding kinetics even for reversible unfolding reactions, we varied heating rates between 0.2 and 2 K/min. However, we could not observe any significant effects on the shape or position of the transition curves. We conclude, therefore, that kinetic effects play no role in the unfolding reaction of His_6HodC. This result is in contrast to what was observed for chitinase 40 (*17*), and it underlines the fact that the differences between the two proteins may be larger than the similarities.

The prominent feature resulting from the analysis of the thermal unfolding profiles of His_6HodC is the occurrence of non-two-state behavior. This characteristic follows unambiguously from the comparison of three unfolding models that were used in the quantitative simulation of the experimental heat capacity curves: the simple two-state approach, the superposition of two independent N ↔ D transitions, and the sequential three-state model. The results are summarized in Figure 3. Inspection of the measured and simulated DSC profile in Figure 3A shows immediately that the two-state N ↔ D model cannot describe the observed data at all. Thus, simple two-state unfolding of HodC can be excluded unambiguously. Figure 3B shows a much better fit. Here the model of two independent two-state transitions was assumed for the analysis. However, an optimal fit is only obtained if a sequential three-state model (N ↔ I ↔ D) is used for the analysis of the DSC curve. This is demonstrated in Figure 3C.

It is worth emphasizing that the improved fit quality is achieved without increasing the number of fit parameters. Therefore, we consider this transition model as being representative for the unfolding mechanism of His_6HodC. We used the thermodynamic parameters resulting from this analysis also for the simulations of the CD spectroscopic and the DSD temperature unfolding profiles, and the high quality fits obtained justified this global approach.

Parameters for the Thermodynamic Characterization of His_6HodC Unfolding by Three States

The three-state analysis of the DSC measurement shown in Figure 3C results in the set of parameters listed in Table 2.

The values of $\Delta H_i°$, $T_{m,i}$, $\Delta C_{p,i}°$, $\partial/\partial T(\Delta C_{p,i}{}^0)$, and $\partial^2/\partial T^2$-$(\Delta C_{p,2}{}^0)$ were used for both the calculation of the stability curves, $\Delta G_i°(T)$, of protein states I and D and the population distributions of the three states. These graphs are shown in panels A and B of Figure 4.

It is obvious that the intermediate state can be formed with little free energy expenditure, and this feature could render it an interesting candidate for mechanistic speculations. Preferential interaction of different substrates with one state of the protein or the other could in principle influence catalytic activity and the compulsory-order mechanism of the reaction. We shall actively study such possibilities in the future. The moderate stability of the enzyme is associated with structural malleability that might be one of the characteristic features involved in ligand binding energy conversion in the catalytic process. Thus, apart from the intrinsic thermodynamic interest, the existence of three states with relatively small Gibbs energy differences opens up a variety of mechanistic implications that are worth studying.

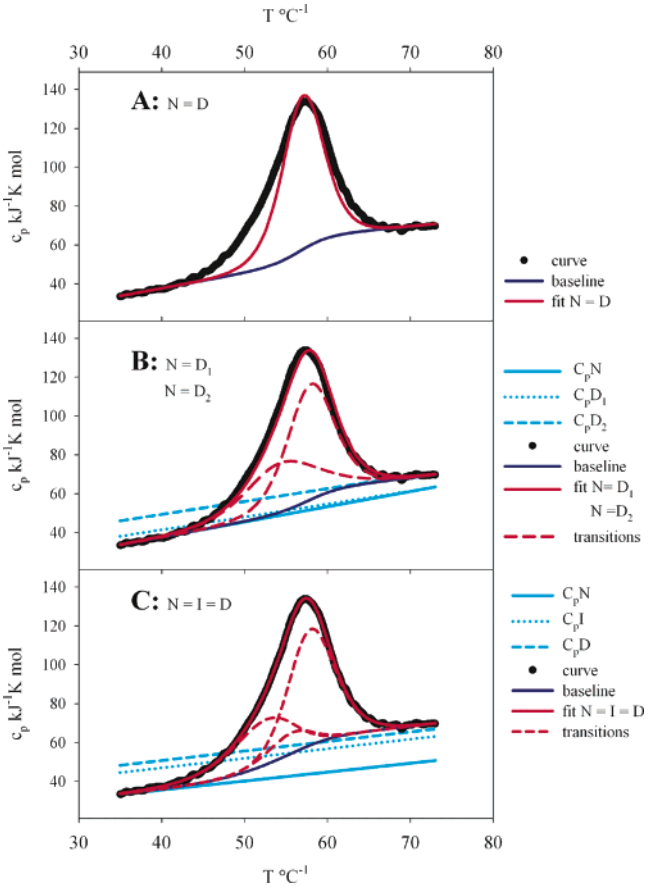

FIGURE 3: Deconvolution of heat capacity curves of His_6HodC. The protein concentration was 1.06 mg/mL, the heating rate 2 K/min, and the buffer 10 mM sodium phosphate buffer (pH 7.5): (●) measurements, (red line) calculated curves, (dark blue line) baselines of measurement, and (light blue solid, dotted, and dashed lines) C_p signals of the pure states N, I, and D, respectively. (A) Data analysis applying a simple two-state model (N ↔ D). The following parameters were used: T_m = 56.9 °C, $\Delta H°(T_m)$ = 533 kJ/mol, $\Delta C_p°(T_m)$ = 12.7 kJ K^{-1} mol^{-1}, $(\partial \Delta C_p°/\partial T)(T_m) = -294$ J K^{-2} mol^{-1}, $(\partial^2 \Delta C_p°/\partial T^2)(T_m) = -6$ J K^{-3} mol^{-1}. (B) Analysis assuming two independent two-state transitions (N ↔ D_1 and N ↔ D_2). The following parameters were used: $T_{m,1}$ = 54.5 °C, $\Delta H°(T_{m,1})$ = 300 kJ/mol, $\Delta C_p°(T_{m,1})$ = 146 J K^{-1} mol^{-1}, $(\partial \Delta C_p°/\partial T)(T_{m,1}) = -121$ J K^{-2} mol^{-1}, $(\partial^2 \Delta C_p°/\partial T^2)(T_{m,1}) = -7$ J K^{-3} mol^{-1}, $T_{m,2}$ = 57.7 °C, $\Delta H°(T_{m,2})$ = 463 kJ/mol, $\Delta C_p°(T_{m,2})$ = 10.2 kJ K^{-1} mol^{-1}, $(\partial \Delta C_p°/\partial T)(T_{m,2}) = -121$ J K^{-2} mol^{-1}, and $(\partial^2 \Delta C_p°/\partial T^2)(T_{m,2}) = -7$ J K^{-3} mol^{-1}. (C) Analysis according to a sequential three-state model (N ↔ I ↔ D). The following parameters were used: $T_{m,1}$ = 53.5 °C, $\Delta H°(T_{m,1})$ = 271 kJ/mol, $\Delta C_p°(T_{m,1})$ = 11.7 kJ K^{-1} mol^{-1}, $(\partial \Delta C_{p,1}°/\partial T) = -2.1$ kJ K^{-2} mol^{-1}, $T_{m,2}$ = 57.5 °C, $\Delta H°(T_{m,2})$ = 461 kJ/mol, $\Delta C_{p,2}$ = 6.7 kJ K^{-1} mol^{-1}, $(\partial \Delta C_{p,2}°/\partial T) = -500$ J K^{-2} mol^{-1}, and $(\partial^2 \Delta C_{p,2}°/\partial T^2) = 3$ mJ K^{-3} mol^{-1}.

CD Measurements. The heat capacity changes monitored by DSC should be associated with corresponding structural changes. Therefore, we followed thermal denaturation of His_6HodC by CD spectroscopy in the far- and near-UV regions. Figure 5A shows the variation with temperature of the mean residue ellipticity $[\Theta]_{MRE}$ at 222 nm which is preferentially reflecting changes in the α-helical structure. Figure 5B shows the corresponding changes in the aromatic region at 295 nm where changes in tertiary structure are monitored. The experimental $[\Theta]_{MRE}$ values represented by the dots can be perfectly fitted when using the population

Table 2: Thermodynamic Transition Properties Characterizing the Sequential Unfolding Reaction (N ↔ I ↔ D) of His_6HodC in 10 mM Sodium Phosphate Buffer (pH 7.5)

	$T_{m,1}$ (°C)	$T_{m,2}$ (°C)	$\Delta H°(T_{m,1})$ (kJ/mol)	$\Delta H°(T_{m,2})$ (kJ/mol)	$\Delta C_p(T_{m,1})$ (kJ K^{-1} mol^{-1})	$\Delta C_p(T_{m,2})$ (kJ K^{-1} mol^{-1})	$\partial/\partial T(\Delta C_{p,1}°)$ (kJ K^{-2} mol^{-1})	$\partial^2/\partial T^2(\Delta C_{p,2}°)$ (mJ K^{-3} mol^{-1})
N ↔ I	53.5		271		11.7		−2.1	
I ↔ D		57.5		461		6.7	−0.5	3.0

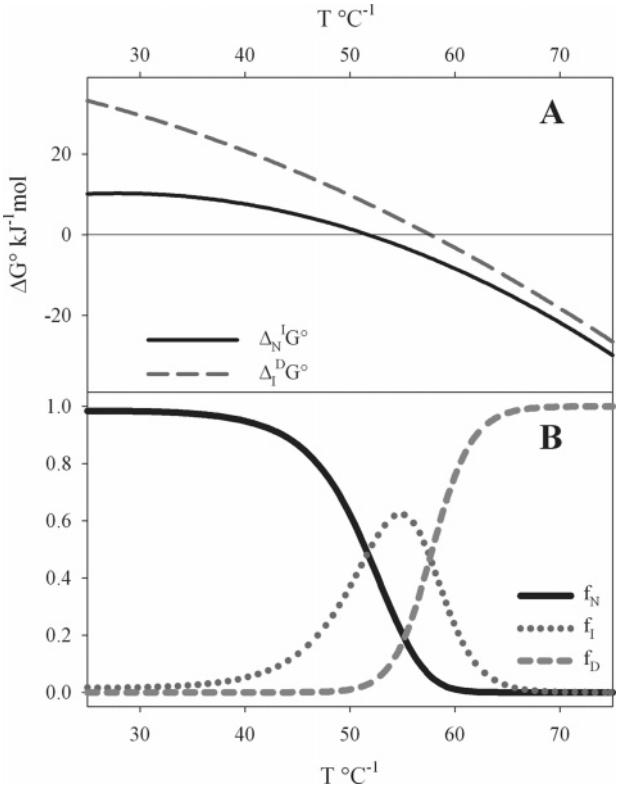

FIGURE 4: Stability curves, $\Delta G°(T)$, of His_6HodC. (A) Functions of the N ↔ I and I ↔ D transitions calculated using the parameters given in Table 2. (B) Representation of the fractions of the native (—), intermediate (···), and denatured states (− − −) of His_6HodC as a function of temperature.

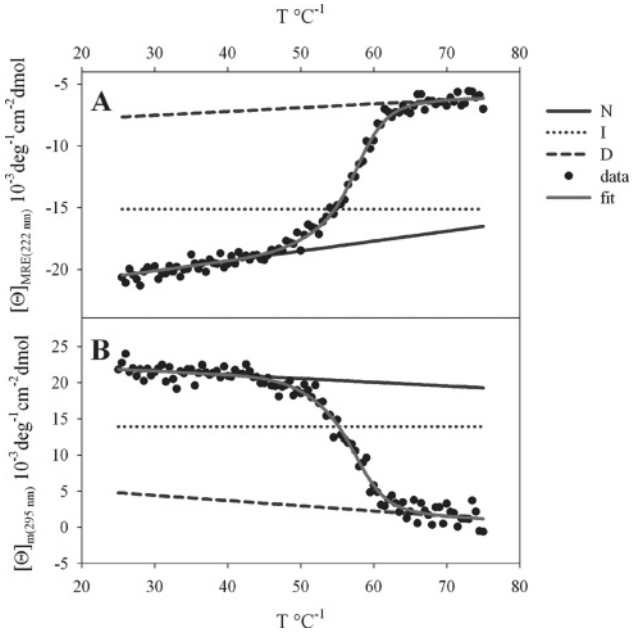

FIGURE 5: CD-monitored thermal transition curves of His_6HodC. The protein concentration was 1.06 mg/mL^{-1}, the buffer 10 mM sodium phosphate (pH 7.5), and the heating rate 2 K/min at (A) λ = 222 nm and (B) λ = 295 nm: (●) measurements, (gray line) calculated curve, and (black line) native, (dotted line) intermediate, and (dashed line) denatured state curves. Population analysis was based on the thermodynamic data obtained from the DSC measurements. The following parameters were used for fitting the linear baselines: $[\Theta]_{MRE,N}$ (222 nm, 25 °C) = −20500 deg cm^2 dmol^{-1}, $d[\Theta]_{MRE,N}$ (222 nm)/dT = 61 deg cm^2 dmol^{-1} K^{-1}, $[\Theta]_{MRE,I}$ (222 nm, 25 °C) = −15100 deg cm^2 dmol^{-1}, $d[\Theta]_{MRE,I}$ (222 nm)/dT = 0 deg cm^2 dmol^{-1} K^{-1}, $[\Theta]_{MRE,D}$ (222 nm, 25 °C) = −7700 deg cm^2 dmol^{-1}, $d[\Theta]_{MRE,D}$ (222 nm)/dT = 42 deg cm^2 dmol^{-1} K^{-1}, $[\Theta]_{m,N}$ (295 nm, 25 °C) = 21800 deg cm^2 dmol^{-1}, $d[\Theta]_{m,N}$ (295 nm)/dT = −51 deg cm^2 dmol^{-1} K^{-1}, $[\Theta]_{m,I}$ (295 nm, 25 °C) = 13900 deg cm^2 dmol^{-1}, $d[\Theta]_{m,I}$ (295 nm)/dT = 0 deg cm^2 dmol^{-1} K^{-1}, $[\Theta]_{m,D}$ (295 nm, 25 °C) = 4700 deg cm^2 dmol^{-1}, and $d[\Theta]_{m,D}$ (295 nm)/dT = −72 deg cm^2 dmol^{-1} K^{-1}.

distributions derived from the DSC studies and the linear baselines of the three states given in the graph. The success of this global analysis is a good indication of the validity of the thermodynamic basis. The resulting $[\Theta]_{MRE}$ values for the three states of the protein at 222 nm as well as their temperature dependence, $d[\Theta]_{MRE}/dT$, are summarized in Table 3.

The data show that the intermediate state retains only ∼42% of the far-UV CD signal of the native state at 25 °C. This indicates a loss of more than 50% of the native secondary structure and implies a drastic change in the α-helical conformation.

The change in tertiary structure with temperature is shown in Figure 5B. The CD changes can again be identified quantitatively when using the same set of thermodynamic data for the calculation of the population changes. The molar ellipticity values ($[\Theta]_m$) at 295 nm for the three states of the protein at 25 °C together with their temperature derivatives are listed in Table 3.

The above CD values for the near-UV region (295 nm) are given as molar ellipticities, whereas the values for the far-UV region (222 nm) were given as mean residue ellipticities, because only the few aromatic side chains contribute to the CD signal in the near-UV region while each side chain (minus one) contributes to the CD peptide bond signal monitored in the far-UV region.

The CD experiments show that with an increase in temperature the tertiary structure of His_6HodC is perturbed in a manner similar to that of the secondary structure. The intermediate state retains ∼46% of the native state signal which is within error limits identical to the value obtained for the change in secondary structure. Thus, when intermediate state I forms from N, we do not have a collapse of tertiary structure with retention of secondary structure, as for example in molten globules, but a synchronous disappearance of secondary and tertiary structure of approximately 44%.

DSD and PMDSC Measurements. The change in apparent molar volume V_m with temperature is presented in Figure 6A. The measured values (dots) indicate already clearly the existence of an intermediate equilibrium state with properties different from those of the native and unfolded states. The experimental curve can again be perfectly fitted

Table 3: Spectroscopic Properties of the Three Thermodynamic States of His_6HodC at 25 °C in 10 mM Sodium Phosphate Buffer (pH 7.5)[a]

state	$[\Theta]_{MRE}$ (222 nm) (deg cm^2 dmol^{-1})	d$[\Theta]_{MRE}$/dT (222 nm) (deg cm^2 dmol^{-1} K^{-1})	$[\Theta]_m$ (295 nm) (deg cm^2 dmol^{-1})	d$[\Theta]_m$/dT (295 nm) (deg cm^2 dmol^{-1} K^{-1})
N	−20500	61	21800	−51
I	−15100	0	13900	0
D	−7700	42	4700	−72

[a] $[\Theta]_m$ is the molar ellipticity at 295 nm characteristic of tertiary structure.

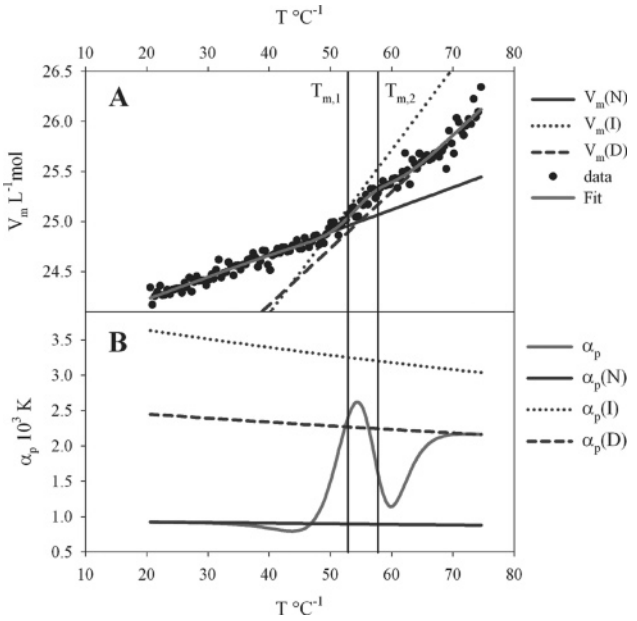

FIGURE 6: Differential scanning density measurements of His_6-HodC. (A) The protein concentration was 2.0 mg/mL, the buffer 10 mM sodium phosphate (pH 7.5), and the heating rate 0.5 K/min. The global analysis was based on the thermodynamic data derived from the DSC measurements: (●) measurements, (gray line) calculated curve, and (black line) native, (dotted line) intermediate, and (dashed line) denatured state curves. The molar volumes of the protein at the midpoint temperatures of the N ↔ I and I ↔ D transitions are as follows: $V(T_{m,1}) = 25.07$ L/mol, and $V(T_{m,2}) = 25.28$ L/mol. (B) Temperature dependence of the isobaric thermal expansion coefficient $[\alpha_p = 1/V(\partial V/\partial T)_p]$ derived from the fitted curve of the molar volume shown in panel A: (gray line) calculated curve and (black line) native, (dotted line) intermediate, and (dashed line) denatured state curves.

on the basis of the global thermodynamic parameters and the linear volume changes of the three states shown in Figure 6A. The intermediate state is characterized by a molar volume at the transition temperature, $T_{m,I}$, that lies above both the volumes of the native and unfolded state.

The expansion coefficient at constant pressure $[\alpha_P = 1/V(\partial V/\partial T)_P]$ was determined from the volume curve by numerical differentiation, and the graph is displayed in Figure 6B. As indicated already in the V_m versus T curve by the slope at $T_{m,I}$, the expansion coefficient of the intermediate state is largest which is in line with the notion of the maximal volume of the pure intermediate state. Accordingly, the expansion coefficient of the enzyme reaches a maximum at $T_{m,I}$ when a maximum of the intermediate state is present. This result reflects the significant changes in interactions and structure associated with corresponding fluctuations that characterize the intermediate state. Characteristic parameters of the three states at 25 °C are summarized in Table 4. Transition values are given at the corresponding transition temperatures.

Table 4: Volumetric Properties of the Three States of His_6HodC in 10 mM Sodium Phosphate Buffer at 25 °C and pH 7.5

state	V_m (L/mol)	α_p ($\times 10^3$ K)	r_H (nm)	$\Delta V_m(T_m)$ (mL/mol)	$\Delta\alpha_p(T_m)$ ($\times 10^3$ K)
N	24.33	0.92	2.3		
I	22.85	3.58	2.5		
D	23.32	2.42	−/−		
N ↔ I				156 (at $T_{m,1}$)	2.6
I ↔ D				−343 (at $T_{m,2}$)	−1.1

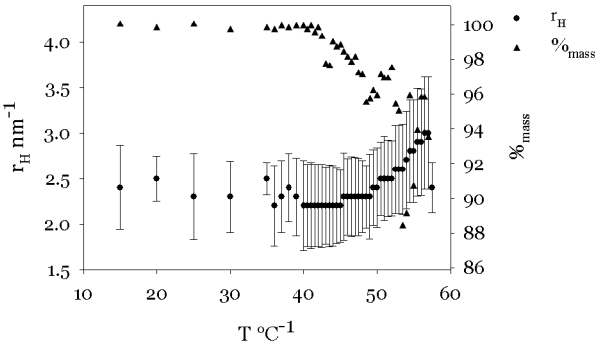

FIGURE 7: Dynamic light scattering measurements of His_6HodC. The hydrodynamic radius, r_H, and the mass percentage of protein associated with r_H as a function of temperature. The protein concentration was 1.0 mg/mL and the buffer 10 mM sodium phosphate (pH 7.5). Each datum point represents the average of 10 measurements; the error bars indicate the polydispersity of the radius distribution: (●) hydrodynamic radius and (▲) mass percentage of the species with the given hydrodynamic radius.

Pressure modulation DSC measurements resulted in a very similar value for the expansion coefficient of the native protein: $\alpha_P(N) = 1.05 \times 10^{-3}$ K^{-1}. However, the expansion coefficients of the two other states could not be determined with reasonable accuracy. This was due to the relatively small difference signal between the PMDSC run with the protein solution and with the reference buffer which precluded proper analysis.

DLS Measurements. Dynamic light scattering was applied to determine the absolute value of and the change in hydrodynamic radius r_H of His_6HodC with temperature. Figure 7 summarizes the results.

The native protein has a hydrodynamic radius of 2.3 nm at 25 °C. The radius remains constant up to ∼50 °C. Then a significant increase is observed. The solid triangles shown in the graph refer to the percentage of mass assigned to species having a radius of 2.3 nm. It is seen that at 40 °C practically 100% of the mass of the protein is associated with the native state radius of 2.3 nm. Above approximately 42 °C, this percentage decreases, indicating the increasing heterogeneity of the system.

The radius can also be estimated from the density measurements. The molar volume of His_6HodC at 25 °C is 24.33 L/mol, and division by Avogadro's number yields the

volume of the individual protein. Assuming a spherical shape, the radius is calculated to be 2.13 nm, which is in good agreement with the measured hydrodynamic radius considering the different approaches.

Packing and hydration appear to change significantly at the transition temperature ($T_{m,1} = 53.5$ °C), as the increase in the experimental hydrodynamic radius to 2.5 nm indicates. Unfortunately, DLS measurements at higher temperatures become increasingly difficult to evaluate due to the complex shape of the autocorrelation function. This may be the result of increased volume fluctuations in the transition region or originate from a loss of homogeneity due to aggregation phenomena that might occur as a result of the relatively long duration of the DLS measurements at the various temperatures.

Conclusions

These thermodynamic, CD spectroscopic, densimetric, and dynamic light scattering studies provided a sound basis for a physicochemical characterization of the unusual dioxygenase Hod. The significance of the thermodynamic stability parameters and the unfolding mechanism derived from heat capacity profiles became particularly evident in their global applicability to the analysis of all thermal unfolding processes independent of the method of detection. Deconvolution of the CD spectra provided the first information for secondary and tertiary structure and their changes with temperature which will have to be tested against X-ray or NMR information once it becomes available. The small free energy differences among the native, intermediate, and unfolded states of the protein allow for speculation concerning specific reactions with different ligands.

REFERENCES

1. Frerichs-Deeken, U., Ranguelova, K., Kappl, R., Hüttermann, J., and Fetzner, S. (2004) Dioxygenases without requirement for cofactors and their chemical model reaction: Compulsory order ternary complex mechanism of 1*H*-3-hydroxy-4-oxoquinaldine 2,4-dioxygenase involving general base catalysis by histidine 251 and single-electron oxidation of the substrate dianion, *Biochemistry 43*, 14485−14499.
2. Fischer, F., Künne, S., and Fetzner, S. (1999) Bacterial 2,4-dioxygenases: New members of the α/β hydrolase-fold superfamily of enzymes functionally related to serine hydrolases, *J. Bacteriol. 181*, 5725−5733.
3. Frerichs-Deeken, U., and Fetzner, S. (2005) Dioxygenases without requirement for cofactors: Identification of amino acid residues involved in substrate binding and catalysis, and testing for rate-limiting steps in the reaction of 1*H*-3-hydroxy-4-oxoquinaldine 2,4-dioxygenase, *Curr. Microbiol. 51*, 344−352.
4. Fetzner, S. (2002) Oxygenases without requirement for cofactors or metal ions, *Appl. Microbiol. Biotechnol. 60*, 243−257.
5. Sambrook, J., Fritsch, E. F., and Maniatis, T. (1989) *Molecular Cloning: A Laboratory Manual*, 2nd ed., Cold Spring Harbor Laboratory Press, Plainview, NY.
6. Eiden, F., Wendt, R., and Fenner, H. (1978) Chinolyliden-Derivate, *Arch. Pharm. (Weinheim, Ger.) 311*, 561−568.
7. Cornforth, J. W., and James, A. T. (1956) Structure of a naturally occurring antagonist of dihydrostreptomycin, *Biochem. J. 63*, 124−130.
8. Laemmli, U. K. (1970) Cleavage of structural proteins during the assembly of the head of bacteriophage T4, *Nature 227*, 680−685.
9. Pace, C. N., Vajdos, F., Fee, L., Grimsley, G., and Gray, T. (1995) How to measure and predict the molar absorption coefficient of a protein, *Protein Sci. 4*, 2411−2423.
10. Boehm, K., Rösgen, J., and Hinz, H.-J. (2006) Pressure-modulated differential scanning calorimetry. An approach to the continuous, simultaneous determination of heat capacities and expansion coefficients, *Anal. Chem. 78*, 984−990.
11. Rösgen, J., and Hinz, H.-J. (2006) Pressure-modulated differential scanning calorimetry: Theoretical background, *Anal. Chem. 78*, 991−996.
12. Häckel, M., Konno, T., and Hinz, H.-J. (2000) A new alternative method to quantify residual structure in 'unfolded' proteins, *Biochim. Biophys. Acta 1479*, 155−165.
13. Häckel, M., Hinz, H.-J., and Hedwig, G. R. (2000) The partial molar volumes of some tetra- and pentapeptides in aqueous solution: A test of amino acid side-chain group additivity for unfolded proteins, *Phys. Chem. Chem. Phys. 2*, 4843−4849.
14. Häckel, M., Hinz, H.-J., and Hedwig, G. R. (2000) Additivity of the partial molar heat capacities of the amino acid side-chains of small peptides: Implications for unfolded proteins, *Phys. Chem. Chem. Phys. 2*, 5463−5468.
15. Böhm, G., Muhr, R., and Jaenicke, R. (1992) Quantitative analysis of protein far UV circular dichroism spectra by neural networks, *Protein Eng. 5*, 191−195.
16. Nardini, M., Ridder, I. S., Rozeboom, H. J., Kalk, K. H., Rink, R., Janssen, D. B., and Dijkstra, B. W. (1999) The X-ray structure of epoxide hydrolase from *Agrobacterium radiobacter* AD1. An enzyme to detoxify harmful epoxides, *J. Biol. Chem. 274*, 14579−14586.
17. Pyrpassopoulos, S., Vlassi, M., Tsortos, A., Papanikolau, Y., Petratos, K., Vorgias, C. E., and Nounesis, G. (2006) Equilibrium heat-induced denaturation of chitinase 40 from *Streptomyces thermoviolaceus*, *Proteins 64*, 513−523.

BI0622423